

## Direct Mapping of Higher-Order RNA Interactions by SHAPE-JuMP

Thomas W. Christy, Catherine A. Giannetti, Gillian Houlihan, Matthew J. Smola, Gregory M. Rice, Jian Wang, Nikolay V. Dokholyan, Alain Laederach, Philipp Holliger, and Kevin M. Weeks\*

Cite This: *Biochemistry* 2021, 60, 1971–1982

Read Online

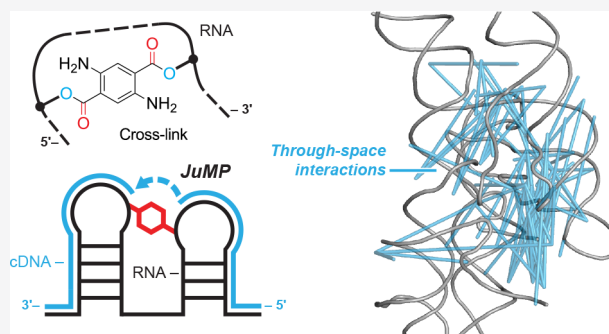
ACCESS |

Metrics & More

Article Recommendations

Supporting Information

**ABSTRACT:** Higher-order structure governs function for many RNAs. However, discerning this structure for large RNA molecules in solution is an unresolved challenge. Here, we present SHAPE-JuMP (selective 2'-hydroxyl acylation analyzed by primer extension and juxtaposed merged pairs) to interrogate through-space RNA tertiary interactions. A bifunctional small molecule is used to chemically link proximal nucleotides in an RNA structure. The RNA cross-link site is then encoded into complementary DNA (cDNA) in a single, direct step using an engineered reverse transcriptase that “jumps” across cross-linked nucleotides. The resulting cDNAs contain a deletion relative to the native RNA sequence, which can be detected by sequencing, that indicates the sites of cross-linked nucleotides. SHAPE-JuMP measures RNA tertiary structure proximity concisely across large RNA molecules at nanometer resolution. SHAPE-JuMP is especially effective at measuring interactions in multihelix junctions and loop-to-helix packing, enables modeling of the global fold for RNAs up to several hundred nucleotides in length, facilitates ranking of structural models by consistency with through-space restraints, and is poised to enable solution-phase structural interrogation and modeling of complex RNAs.



RNA plays key biological roles as ribozymes, translation regulators, scaffolding centers, and ligand binders. These fundamental regulatory functions often occur when an RNA folds into complex secondary and tertiary structures.<sup>1–3</sup> Discovering and defining these structures provide insights into how RNA molecules function. Chemical probing is a powerful approach for mapping RNA structure at large scales and in a sufficiently unbiased way as to be useful as a function discovery tool.<sup>4</sup> Strategies for chemical probing of RNA secondary structure, especially using selective 2'-hydroxyl acylation analyzed by primer extension and mutational profiling (SHAPE-MaP),<sup>5,6</sup> DMS-MaP,<sup>7,8</sup> and single-molecule correlated chemical probing (RING) methods,<sup>7,9,10</sup> are transforming our understanding of RNA structure–function interrelationships. The broad applicability and accuracy of these methods reflect, in large part, strategies in which the sites of chemical modification in RNA are read out in a complementary DNA (cDNA) in a single direct step. A key insight from prior work emphasizes that methods that detect chemical modifications in RNA directly are superior to those that require multiple intervening biochemical steps.<sup>11–13</sup>

Here, we introduce a concise strategy for mapping tertiary and higher-order RNA–RNA interactions across large RNA molecules, SHAPE-JuMP (selective 2'-hydroxyl acylation analyzed by primer extension and juxtaposed merged pairs). SHAPE-JuMP monitors tertiary structure via a bireactive SHAPE chemical cross-linking reagent that reacts preferentially with the 2'-hydroxyl groups of two nucleotides in the

proximity of each other (Figure 1). An engineered reverse transcriptase (RT), effectively a reverse transcriptase, then “jumps” across the cross-link to permanently record the cross-link site as a deletion in the resulting cDNA strand. The ability to traverse chemical cross-links required an engineered enzyme, RT-C8,<sup>14</sup> which was optimized from a reverse transcriptase previously shown to be permissive toward alternative nucleic acid backbones.<sup>15</sup> Locations of cross-link-induced deletions are identified by aligning sequencing reads to a reference sequence. We show these internucleotide cross-links report long-range through-space interactions in complex RNA structures, useful for higher-order structure discovery and modeling.

### RESULTS

**TBIA Cross-Links RNA.** We created a new bifunctional SHAPE reagent, *trans*-bis-isatoic anhydride (TBIA), to cross-link RNA nucleotides (Figure 2A). TBIA has two electrophilic isatoic anhydride moieties, each of which can react with the nucleotide 2'-OH group. When TBIA reacts with one

Received: April 20, 2021

Revised: May 27, 2021

Published: June 14, 2021



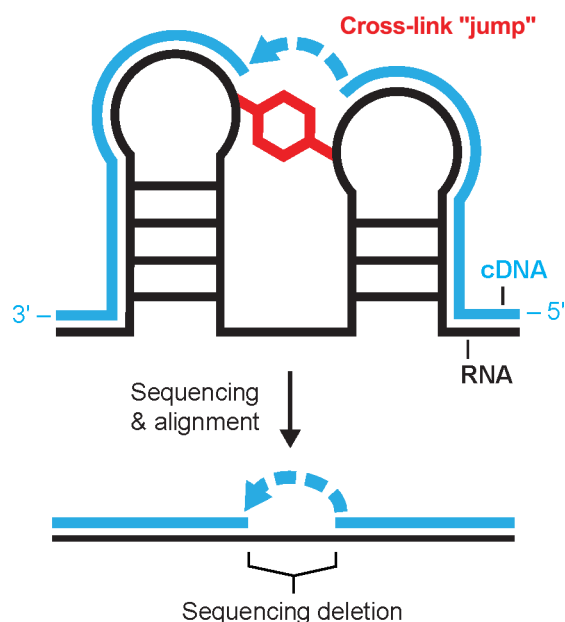


**Figure 1.** SHAPE-JuMP overview. RNA is treated with a bivalent SHAPE cross-linker (red), which covalently links proximal nucleotides. Reverse transcription using an engineered jumping, or cross-link-traversing, polymerase records the cross-linked site as a deletion in the cDNA (blue). The cDNA is sequenced and aligned to the reference RNA sequence to identify deletion sites and, thereby, cross-linked nucleotides.

nucleotide, its second anhydride moiety can react with a second, proximal, nucleotide, forming a covalent cross-link. Cross-links can occur between nucleotides both adjacent to and distant in the primary RNA sequence as long as they are in close three-dimensional physical proximity. SHAPE reagents, like TBIA, react with all four nucleotides.<sup>5</sup> TBIA will also form monoadducts when one anhydride reacts with a nucleotide, but the second anhydride is hydrolyzed by water. To distinguish monoadduct formation from true cross-links, we compared SHAPE-JuMP signals due to TBIA with monoadducts created using isotopic anhydride (IA) (Figure 2A), a molecule with a structure similar to that of TBIA but with only one reactive group.

To examine the ability of TBIA to cross-link RNA, we folded RNA transcripts with the sequence of the *Bacillus stearothermophilus* RNase P catalytic domain<sup>16</sup> or the A756G mutant of the Varkud satellite (VS) ribozyme<sup>17</sup> and treated each with TBIA. Product formation was visualized by denaturing gel electrophoresis as a lower-mobility band absent in no-reagent and IA-treated controls (Figure 2B and Figure S1). TBIA induced efficient cross-linking (5–10%) in each RNA, and cross-linking was independent of RNA concentration, indicating that cross-links reflected intramolecular interactions (Figure S1). To establish optimal reaction times for cross-linking RNA with TBIA, we followed TBIA hydrolysis by monitoring the change in ultraviolet (UV) absorbance at 296 nm (Figure 2C). The time decay fit a double-exponential function, consistent with two-site reactivity

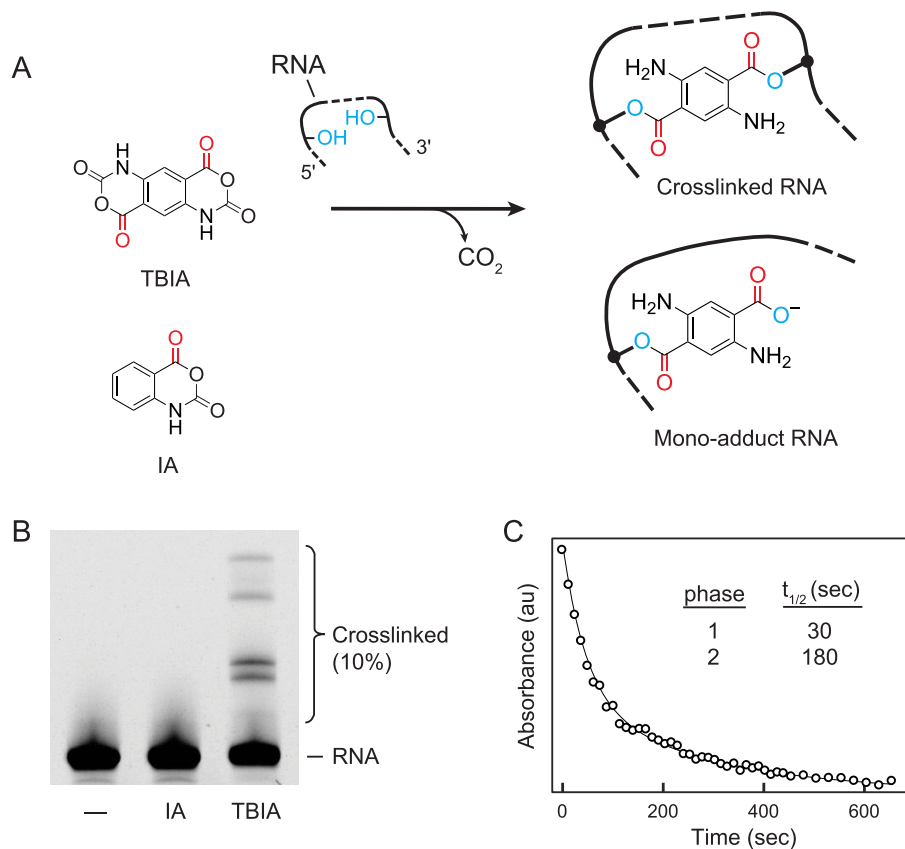


**Figure 2.** TBIA mechanism and characterization. (A) Reaction of TBIA with RNA yields both cross-links and monoadducts. IA strictly forms monoadducts. (B) Reaction of the RNase P RNA with no reagent (–), IA (monoadduct), or TBIA (cross-linking reagent), visualized by denaturing electrophoresis. (C) Hydrolysis of TBIA in a buffer. The reaction was monitored by ultraviolet absorbance at 296 nm; the absorbance as a function of time was fit to a double-exponential rate equation.

by TBIA, and half-lives ( $t_{1/2}$ ) of 30 and 180 s. We implemented cross-linking using a reaction time of 15 min, corresponding to five half-lives of the slower reaction.

**Identification of an Efficient Cross-Link-Traversing RT.** We tested diverse RT enzymes for their ability to use a cross-linked RNA as template. These enzymes included a processive mutant of Moloney murine leukemia virus RT (similar to SuperScript II), Marathon RT,<sup>18</sup> and multiple enzymes created by directed evolution.<sup>14,15</sup> We treated the RNase P catalytic domain RNA with either the TBIA cross-linker or *N*-methyl IA (NMIA, which creates monoadducts), generated and sequenced cDNA transcripts, aligned these sequences to the parent sequence, and quantified the deletions that formed in the TBIA and NMIA experiments for each polymerase. We found many enzymes had modest apparent jumping ability, but the most useful enzyme was RT-C8,<sup>14</sup> which consistently showed 3-fold higher absolute rates of deletion detection for TBIA over the NMIA background (Figure 3). The observed deletion detection rate for TBIA over

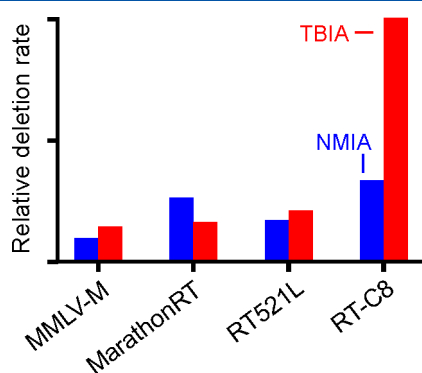


**Figure 3.** Identification of reverse transcriptase enzymes with the ability to jump RNA cross-links. Comparison of cross-link detection in the RNase P RNA by different RT enzymes. Deletion rates for RNAs treated with TBIA and monoadduct-forming NMIA reagents are red and blue, respectively.

an IA background is 1–3%, while 5–10% of RNAs form low-mobility bands as visualized physically by denaturing gel electrophoresis (Figure 2B and Figure S1); cross-link detection by RT-C8 is thus roughly 30% efficient. RT-C8 was used for all subsequent experiments.

**SHAPE-JuMP of RNAs with Complex Structures.** We evaluated the ability of SHAPE-JuMP to detect nucleotides in the proximity by analyzing RNAs with complex structures: the *Tetrahymena thermophila* group I intron P546 domain (P546, 158 nucleotides),<sup>19</sup> the aforementioned VS ribozyme (186 nucleotides)<sup>17</sup> and RNase P catalytic domain (268 nucleotides)<sup>16</sup> RNAs, and the *Oceanobacillus iheyensis* group II intron<sup>20</sup> (group II, 412 nucleotides). We note that while the VS RNA construct forms a dimer at high concentrations,<sup>17</sup> it forms cross-links in a concentration-independent manner over the range of 0.5–2  $\mu$ M, consistent with the formation of a monomer under our conditions (Figure S1). These RNAs form diverse structures. P546 adopts a simple tertiary structure involving close packing of two sets of extended helices; the VS ribozyme has a distinct fold but does not form a compact tertiary structure with closely spaced helices and has served as a target in the RNA-Puzzles structure prediction exercise,<sup>21</sup> and RNase P and the group II intron form complex structures and are much larger than can be confidently modeled using

current methods. These RNAs allowed us to examine SHAPE-JuMP across diverse structural motifs and degrees of complexity.

Each RNA was transcribed *in vitro* and refolded under conditions that support native tertiary structure formation. Folded RNAs were then treated with TBIA. The RT-C8 polymerase has a distinctive and valuable cross-link-traversing activity; however, this polymerase does induce mutations and deletions when copying RNA templates that do not contain cross-links. We controlled for these background deletions by comparing TBIA reactions with parallel experiments performed with IA (Figure 2A). All TBIA-treated RNAs showed 2–5-fold higher per-read deletion rates than samples treated with IA (Figure S2), suggesting that a majority of deletions detected in TBIA-treated samples correspond to cross-links resulting from proximal nucleotides rather than the background activity of the RT enzyme. We created a specialized alignment algorithm that accounts for the complex observed deletion and sequence mutation patterns (Figure S2B) to accurately map TBIA-induced deletion sites and rank these by frequency.<sup>22</sup> RT-C8 does not detect monoadducts as IA-treated, and no-reagent experiments showed similar deletion rates (Figure S2) and positions (Figure S3). Full experimental replicates showed highly correlated deletion rates, similar deletion sites across replicates, and similar through-space distance distributions (Figure S4). We observed cross-links involving all four ribonucleotides, consistent with the expected predominant reaction at the 2'-hydroxyl group.<sup>5,6</sup>

We next characterized deletion lengths as quantified in the cDNAs generated by RT-C8. Across all RNAs, average observed (background) deletion lengths in IA-treated samples were <50 nucleotides, while deletion lengths in TBIA-treated RNAs varied as a function of RNA structure. For the relatively unstructured VS RNA, deletion lengths for IA and TBIA were similar, whereas for the highly structured RNase P (Figure 4A) and group II intron (Figure S5A), deletion distances in TBIA-treated samples were much longer than those in the IA-treated controls. As measured by RT-C8, TBIA-induced deletion lengths are thus related to the extent of structure in an RNA, but non-cross-link-induced deletions are not.

We next examined the physical distances between nucleotides mapped in the JuMP step as a function of cross-link frequency and RNA. For all RNAs, cross-link frequency correlated with a shorter through-space distance (Figure S5D). The most frequent 3% of deletions were between nucleotides separated in space by a mean distance of 21–26 Å, upon comparison to the accepted structure for each RNA (Figure 4B). These distances are significantly shorter than those obtained from random sampling, including after controlling for the sequence length distributions of the TBIA-derived internucleotide pairs (Kolmogorov–Smirnov test, all  $p$  values of  $<10^{-5}$ ). Across all four RNAs, 78% of the distances are <30 Å, which we accept as true positive measurements. We also observe a small fraction, 4%, of distances of  $\geq 45$  Å, which likely reflect some combination of false positive measurements, conformational dynamics in these large RNAs, or other features not reflective of internucleotide distances (see ref 22). We additionally compared deletions detected for the RNase P RNA in the presence and absence of  $Mg^{2+}$ , an ion essential for native tertiary folding.<sup>16,23</sup> Probing in the absence of  $Mg^{2+}$  yielded a deletion distribution markedly different from that of the fully folded structure and roughly comparable to the

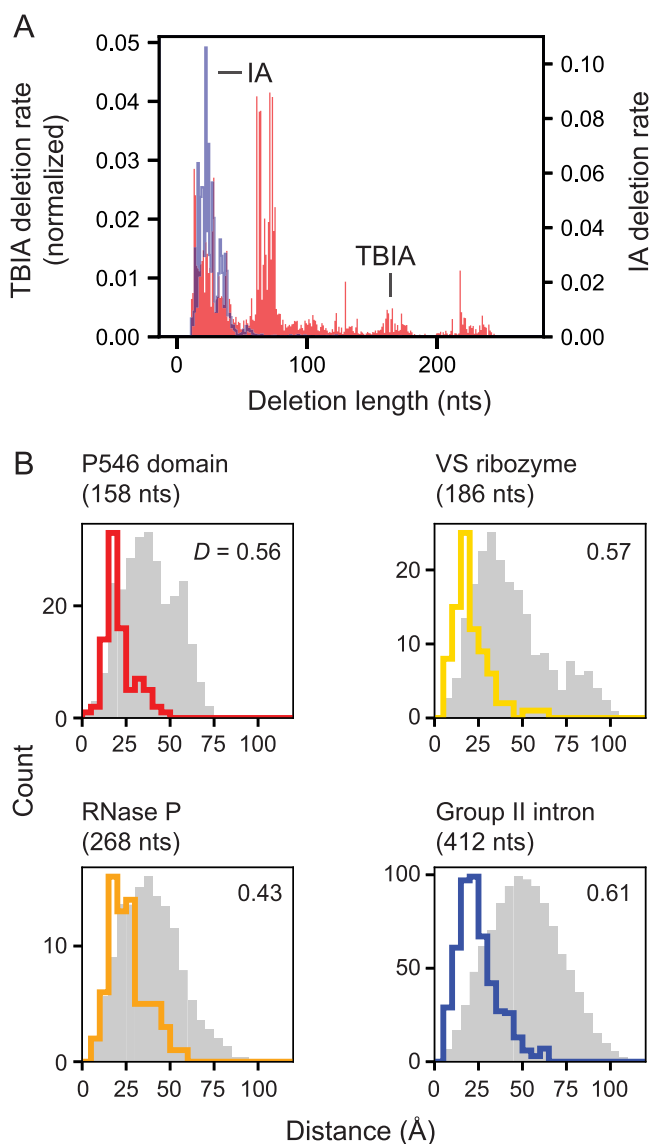


**Figure 4.** SHAPE-JuMP deletion detection as a function of intervening sequence length and through-space distance. (A) Deletion rates of a given length due to treatment with monoadduct-forming IA and cross-linker TBIA for the RNase P RNA. Deletion rates are normalized to sum to 1. (B) Distances between nucleotides that mediate TBIA-induced deletions. The most frequent 3% of deletion rates are shown with colored lines. Random internucleotide distances based on the reference structure, which follow the same sequence length distribution as TBIA-induced contacts, are colored gray. *D*, the Kolmogorov–Smirnov metric, quantifies the separation between two distributions on a scale of 0–1, with 0 indicating no separation and 1 indicating complete separation. All *D* values correspond to *p* values of  $\leq 10^{-5}$ .

result expected for random sampling of through-space interactions (Figure 5).

In summary, these data emphasize that SHAPE-JuMP detects proximal through-space interactions at nanometer resolution and, when native interactions are destabilized by omitting  $Mg^{2+}$ , the resulting cross-links capture interactions characteristic of alternative states. Three experimental heuristics facilitate reliable identification of through-space tertiary RNA–RNA internucleotide interactions using the current JuMP strategy. (i) Samples should be sequenced to a

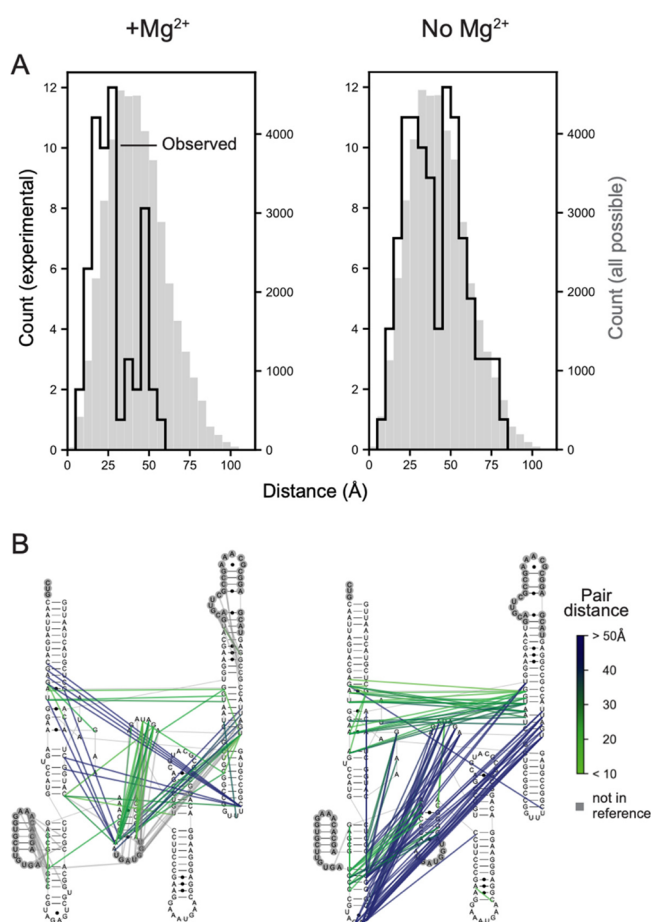


**Figure 5.** SHAPE-JuMP interactions detected for the RNase P RNA in the presence and absence of  $Mg^{2+}$ . (A) SHAPE-JuMP interactions for the most frequent 3% of deletions for RNase P in the presence (left) and absence (right) of  $Mg^{2+}$ . Experimentally measured distances are shown with black lines; gray histograms represent distances of all nucleotide pairs in the reference structure. (B) Internucleotide cross-links, detected as cDNA deletions, superimposed on the secondary structure, colored by through-space distance as calculated from the reference structure.<sup>16</sup> Nucleotides not visualized in the reference structure are shown within gray circles.

minimum read depth of 500000 reads. (ii) The deletion rate for the cross-linked sample should be at least 2-fold higher than that of a no-reagent or monoadduct control. (iii) The overall cross-link-mediated deletion rate should be  $>0.01$  deletion per read.

**SHAPE-JuMP Identifies Diverse, Specific Internucleotide Interactions.** Cross-linked nucleotides identified by SHAPE-JuMP tend to involve at least one unpaired RNA region, consistent with the preferential reactivity of SHAPE reagents for conformationally flexible sites in RNA. Nonetheless, many cross-links are recorded between an unpaired region and a base-paired region, likely partially because the second reactive group in TBIA can react with structurally diverse nearby nucleotides due to an increased effective local concentration. For example, in P546, interactions extend from single-stranded regions adjacent to helix P6a to the base-paired region in P4 (Figure 6A). Similar patterns are observed in the group II intron, for example, between the ID2 loop and the IC helix (Figure 6D).

In the test set of RNAs, SHAPE-JuMP detected internucleotide interactions within every multihelix junction, as

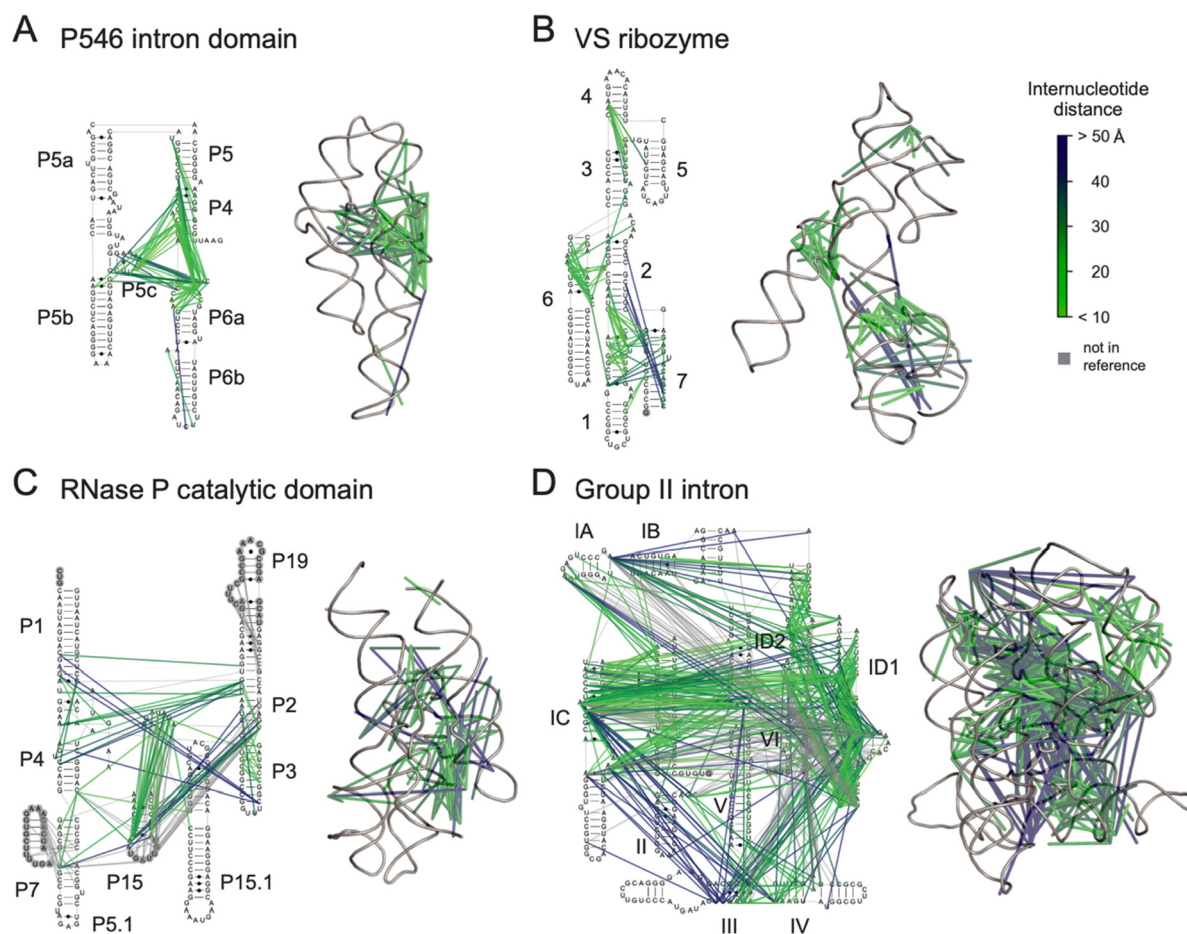


**Figure 6.** Visualization of SHAPE-JuMP interactions on complex RNA structures. Through-space interactions, detected as cDNA deletions, superimposed on secondary and tertiary structure models of (A) the P546 intron domain<sup>19</sup> (PDB entry 1gid), (B) the VS ribozyme<sup>17</sup> (4r4p), (C) the RNase P catalytic domain<sup>16</sup> (3dhs), and (D) the group II intron<sup>20</sup> (3igi). Internucleotide interactions are shown as lines, colored by through-space distance. Interactions are shown for the most frequent 3% of measured deletions. Nucleotides not visualized in three-dimensional structure models are denoted with gray circles.

exemplified by the helix 1–2–7 three-helix junction of the VS ribozyme (Figure 6B) and the helix III–IV–V junction of the group II intron (Figure 6D). We also identified internucleotide interactions between the single-stranded regions of junctions and their connected helices, as exemplified by the helix 3–4–5 junction of the VS ribozyme (Figure 6B) and the helix P1–P3–P4 junction of RNase P (Figure 6C). Internucleotide interactions identified by SHAPE-JuMP are thus not limited to base-paired or single-stranded nucleotides or to a specific structural motif and are particularly common in multihelix junctions.

A majority of SHAPE-JuMP internucleotide interactions occur in clusters, as is readily visualized when contacts are mapped onto the known secondary and tertiary structures (Figure 6). This clustering increases confidence that true proximal through-space interactions are identified by SHAPE-JuMP. Clusters occur throughout the tested RNAs and in both solvent-accessible and inaccessible regions, as supported by comparing the solvent-accessible surface areas of each nucleotide 2'-OH group to the total deletion rate at each nucleotide (Figure S6). This observation is consistent with prior work that demonstrated that SHAPE reactivity is not governed by solvent accessibility.<sup>24</sup> Thus, SHAPE-JuMP identifies proximal through-space interactions in the interior and exterior of RNAs with complex structures.

**SHAPE-JuMP-Restrained Structure Modeling.** *De novo* RNA structure modeling is improving rapidly but remains challenging for large RNAs.<sup>21,25</sup> Experimental restraints can dramatically improve physics-based modeling,<sup>7,26,27</sup> and SHAPE-JuMP identifies through-space RNA–RNA interactions with mean distances on the sub-25 Å scale (Figure 4), roughly corresponding to the width of an RNA helix. We therefore explored the usefulness of SHAPE-JuMP measurements for reducing the conformational space sampled during tertiary structure modeling. SHAPE-JuMP restraints can, in principle, be incorporated into any modeling framework. Here, we explored the impact of SHAPE-JuMP restraints using discrete molecular dynamics (DMD)<sup>28,29</sup> to model the global folds of the RNAs examined in our study. We represent the RNA structure in a simplified way for DMD simulations. Each nucleotide is modeled as three beads, corresponding to the phosphate, ribose, and nucleobase. SHAPE-JuMP restraints were incorporated by applying an energy bonus to the subset of DMD models during a simulation in which cross-linked nucleotides are within specified distance thresholds.<sup>7,29</sup>

Restraints were applied in three steps during the DMD simulation, motivated by both the classes of internucleotide interactions directly measured by SHAPE-JuMP and the hierarchical nature of RNA folding.<sup>30</sup> In step 1, secondary structure restraints, corresponding to canonical base pairing,

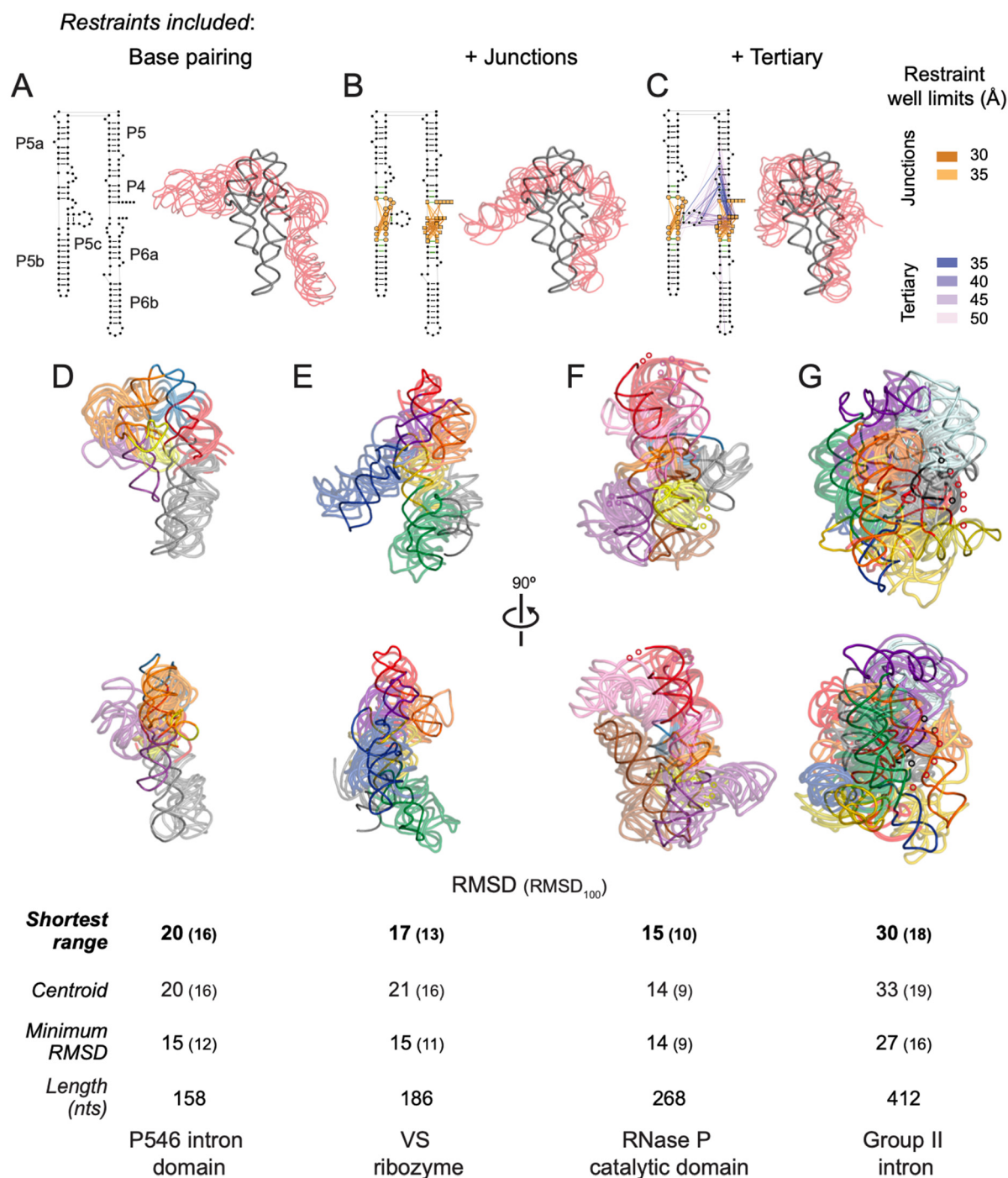


**Figure 7.** SHAPE-JuMP directed structure refinement. (A–C) Restraints superimposed on secondary structure and resulting three-dimensional models for the stepwise DMD refinement of the P546 intron domain. Five modeled structures (transparent red), consisting of the centroid and four models with the lowest RMSD compared to this centroid, aligned with the reference structure<sup>19</sup> (gray) are shown. Restraints were added stepwise, (A) starting with the base-paired secondary structure, (B) adding SHAPE-JuMP restraints at multihelix junctions (orange lines), and (C) adding high-frequency proximity interactions (purple lines). Lengths of restraint wells used during DMD refinement are color-coded. Structures obtained using JuMP data-informed DMD aligned with the (D) P546 domain (PDB entry 1gid), (E) VS ribozyme (4r4p), (F) RNase P catalytic domain (3dhs), and (G) group II intron (3igi). JuMP restraints were mapped onto final models. The five models with the shortest restraint distance ranges were taken as being representative of the simulation. Structures are colored by major helical elements. Modeled and accepted structures are shown with transparent and solid backbone traces, respectively. RMSD values are shown for models with the shortest restraint distance range, the centroid of the largest cluster, and the lowest-RMSD model obtained. RMSD<sub>100</sub> values (in parentheses) report a length-normalized RMSD.<sup>33</sup> Regions not visualized in accepted structures are denoted with small spheres.

were applied (Figure 7A). Accurate secondary structure models for most RNAs are readily obtained by SHAPE-MaP and PAIR-MaP chemical probing<sup>9,31</sup> and were available for

each RNA in the test set.<sup>6,31,32</sup> This step did not use SHAPE-JuMP data. In step 2, restraints corresponding to SHAPE-JuMP interactions identified within multihelix junctions were

added (Figure 7B, orange and yellow lines). In step 3, SHAPE-JuMP-informed restraints corresponding to through-space tertiary structure proximity were added (Figure 7C, blue and purple lines). Restraints corresponding to the most frequently measured deletions were awarded bonuses at shorter distances (Figure 7C and Figure S5D). A final representative model was obtained from step 3 by selecting the model most consistent with the SHAPE-JuMP data: we calculated distances between SHAPE-JuMP-connected nucleotides for the junction and tertiary restraints for each RNA and selected the model with the shortest range of restraint distances.

SHAPE-JuMP-directed refinement yielded final models with root-mean-square deviation (RMSD) values ranging from 15 to 30 Å, relative to the accepted structure, with longer molecules having larger RMSD values, as expected (Figure 7D–G). Models show marked improvements in RMSD after modeling steps 2 and 3, emphasizing the value of solution-phase SHAPE-JuMP restraints (Table S1). RMSD values normalized to a length of 100 nucleotides<sup>33</sup> (RMSD<sub>100</sub>) fell into a narrow range of 10–18 Å. For P546, the three groups of SHAPE-JuMP restraints yielded a refined model that captured the overall structure of the RNA with the exception of the P5b region, which lacked proximity interactions linking it to the rest of the structure (Figure 7D). For VS, the refined model clearly captured the global architecture of the reference structure (Figure 7E). RNase P was an especially favorable case, as the overall fold and helix positions were in good agreement with the accepted structure (Figure 7F). Similarly, the SHAPE-JuMP-directed model of the group II intron has the correct boxlike shape of the accepted structure<sup>34</sup> and correctly places the helices comprising the catalytic core in the center of the structure (Figure 7G).

## DISCUSSION

SHAPE-JuMP embraces two distinctive findings informed by our previous work. First, experience with other RNA structure-probing technologies has revealed that the sensitivity and accuracy for detection of chemical adducts in RNA are strongly dependent on the directness of the strategy used to record the chemical event in a sequencing readout. In SHAPE-JuMP, sites of cross-linking are read out in a single direct step in which an engineered reverse transcriptase extends through a cross-link site and permanently records this site as a deletion in the synthesized cDNA. Second, the cross-linking reagent, TBIA, reacts preferentially with a generic site in the RNA, the 2'-hydroxyl, such that nearly all high-frequency cross-links report higher-order internucleotide proximity corresponding to multihelix junctions, through-space helix packing, and other tertiary interactions.

SHAPE-JuMP thus has unique features relative to the current generation of cross-linking approaches, which are read out by high-throughput sequencing. Several approaches for identifying RNA–RNA interactions use UV-mediated psoralen cross-linking and primarily detect secondary structure.<sup>35–40</sup> For psoralen-based methods, cross-link sites are read out by multistep ligation strategies, and psoralen shows marked sequence and structural preferences.<sup>11,38,39,41</sup> Psoralen-based methods have the notable advantage of being successfully used in cells and the ability to detect long-range and intermolecular interactions. There are also several information-rich strategies for mapping through-space interactions that employ extensive mutagenesis of<sup>29,42</sup> or introduction of pre-structure-probing chemical modifications into<sup>43,44</sup> RNA transcripts. These

methods are complex to implement that, to date, has reduced their wide adoption.

The JuMP strategy is thus unique in its experimental directness and concision, can read out multiple classes of cross-links (including those induced by TBIA, psoralen, and UV irradiation),<sup>22</sup> and will likely prove a foundational approach for future high-throughput RNA tertiary structure discovery technologies. Current limitations include that SHAPE-JuMP does not detect all tertiary contacts in the benchmark RNAs and the fraction of false positive interactions merits improvement. In addition, SHAPE-JuMP currently works best in an amplicon format in which RNA-specific primers are used to amplify a defined sequence. These limitations can likely be addressed by the development and use of alternative cross-linking reagents and by further optimization of the jumping activity of the RT-C8 polymerase. SHAPE-JuMP in its current form has the potential to detect very long-range and intermolecular interactions in RNA, which can be examined using alternative benchmarking systems.

Median through-space distances measured by SHAPE-JuMP are ~23 Å. This distance is independent of the size of the RNA in our test set, which range in length from 158 to 412 nucleotides. The 23 Å distance is comparable to the width of an RNA helix but longer than the 7 Å distance between the reactive carbonyl sites in TBIA, indicating that detection of through-space interactions is governed, in part, by features beyond simple physical proximity, likely reflective of RNA flexibility and dynamics. SHAPE-JuMP has a strong propensity for identifying two classes of through-space interactions. First, SHAPE-JuMP detected multiple interactions across every multihelix junction present in the RNAs of known structure evaluated here (10 junctions across four RNAs). This property of SHAPE-JuMP will likely prove impactful in future work as RNAs with multihelix junctions are overrepresented among functional RNAs. Second, SHAPE-JuMP measures through-space interactions between an unpaired loop and either a second loop or a closely packed helix. These interactions are especially valuable in modeling large RNAs with globular folds.

In this study, we focused on large RNAs that are generally difficult to model *de novo*. There are two core challenges in modeling RNA structure in solution, and SHAPE-JuMP makes a useful contribution to each. SHAPE-JuMP cross-links can be used, first, as restraints for modeling three-dimensional RNA folds and, second, to rank models created by modeling. The VS ribozyme modeled in our study was a target in the RNA-Puzzles competition, whose entries spanned a  $26 \pm 6$  Å RMSD, with the best model yielding a 20 Å RMSD.<sup>21</sup> Our SHAPE-JuMP-directed modeling and selection strategy yielded a structure for the VS ribozyme with a 17 Å RMSD, outperforming the best RNA-Puzzles model. Selecting the best final model by assessing agreement with SHAPE-JuMP restraints was important and improved the model accuracy from 21 to 17 Å RMSD, relative to simply selecting the centroid of the lowest-energy cluster (Figure 7E). The RNase P and group II intron RNAs are considerably longer than those either available in the RNA-Puzzles competition or generally attempted by *de novo* modeling. SHAPE-JuMP-restrained DMD modeling outperformed prior data-driven modeling efforts for the RNase P catalytic domain (including prior work from our lab)<sup>7,45,46</sup> and for variants of the group II intron.<sup>47,48</sup>

There are two additional promising features of SHAPE-JuMP-directed interrogation of large-scale RNA structure. First, VS lacks long-range tertiary interactions and has an

extended topology, and SHAPE-JuMP did not detect tertiary structure where none exists. Second, modeling accuracy, as measured by the length-normalized RMSD<sub>100</sub>, fell in a compact range, 10–18 Å, despite the variety of architectures modeled and the large sizes of the RNase P (268 nucleotides) and group II intron RNAs (412 nucleotides). These insights suggest that the concise SHAPE-JuMP experiment, coupled with restraint-directed modeling, will specifically prove useful for the discovery and modeling of large RNA architectures in viral RNAs, mRNAs, and long noncoding RNAs.

## METHODS

**TBIA Synthesis.** A sample of 500 mg (2.55 mmol) of 2,5-diaminoterephthalic acid (Sigma-Aldrich catalog no. 717312) was dissolved in 11 mL of fresh anhydrous dioxane (Acros Organics) under nitrogen in a stirred three-neck round-bottom flask with a condenser. Next, 0.5 mL (4.18 mmol) of diphosgene was added dropwise, and the flask was heated to 90 °C for 2 h. A second addition of 0.25 mL (2.09 mmol) of diphosgene was added dropwise; the temperature increased to 95 °C, and the reaction continued for a further 3 h. The reaction mixture was then chilled to 4 °C in an ice bath, precipitating the product. The precipitate was filtered in a vacuum flask, washed several times with anhydrous diethyl ether, and dried under vacuum at room temperature. Reactions using diphosgene were performed in a hood that functioned well, and all waste was neutralized with a saturated sodium bicarbonate solution. The final product was a green solid, in 70% yield [<sup>1</sup>H NMR (*D*<sub>6</sub>-DMSO) δ 11.9 (2 NH s), 7.6 (2 ArH s)].

**TBIA Hydrolysis.** Hydrolysis rates were determined by UV (Nanodrop 2000) in a cuvette preheated to 37 °C. Reactions were initiated by adding 900 μL of prewarmed 1× folding buffer [100 mM HEPES (pH 8.0), 100 mM NaCl, and 10 mM MgCl<sub>2</sub>] to 100 μL of 40 nM TBIA in DMSO. Spectra were recorded continuously for 11 min. During this time period, a narrow peak at 296 nm was lost, and a broad peak centered at 425 nm shifted to 395 nm. The absorbance at 296 nm was biphasic, consistent with two hydrolysis processes for the reaction; a double-exponential decay model was used to fit (Prism 8) the data:

$$Y = (Y_0 - Y_{\text{final}})(f_{\text{fast}})e^{-k_{\text{fast}}t} + (Y_0 - Y_{\text{final}})(1 - f_{\text{fast}})e^{-k_{\text{slow}}t}$$

where  $Y_0$  and  $Y_{\text{final}}$  are the initial and final absorbance, respectively,  $f_{\text{fast}}$  is the fraction of the signal associated with the fast rate (ideal = 0.5),  $k_{\text{fast}}$  and  $k_{\text{slow}}$  are the rate constants for each of the sites, and  $t$  is the time in seconds.

**Reverse Transcriptase Polymerase.** The reverse transcriptase RT-C8 was selected using *in vitro* mutagenesis and optimized using compartmentalized bead labeling<sup>14</sup> starting with the previously developed relaxed fidelity, XNA incorporating, reverse transcriptase RT521K,<sup>15</sup> itself derived from the *Thermococcus gorgonarius* replicative polymerase.<sup>49,50</sup> Large-scale expression and purification of RT-C8 was performed as described previously.<sup>51</sup> Briefly, RT-C8 was expressed in BL21 CodonPlus-RIL *Escherichia coli* cells (Agilent Technologies); protein expression was induced in mid log phase (OD<sub>600</sub> = 0.4–0.6) with anhydrotetracycline (final concentration of 0.4 μg/mL) for 4 h at 37 °C. A 1 L culture was harvested by centrifugation and resuspended in 10 mL of lysis buffer A [50 mM Tris-HCl (pH 7.4) and 1% (w/v) glucose] with 30 mL of lysis buffer B [10 mM Tris-HCl (pH 7.4), 50 mM KCl, 0.5%

NP40, and 0.1% Triton X-100] and 10 mL of 5 M NaCl and lysed by incubation at 75 °C for 30 min. Cell debris were pelleted by centrifugation, and the lysate was diluted 20-fold with running buffer [50 mM NaCl, 10% glycerol, 0.02% NaN<sub>3</sub>, and 20 mM Tris-HCl (pH 7.4)] and loaded onto a DEAE Sephadex A-25 column (GE Life Sciences) equilibrated in running buffer. The flow-through was collected and loaded directly onto an equilibrated HiPrep Heparin FF 16/10 column (GE Life Sciences). The heparin column was washed with running buffer, and a linear gradient from 50 mM to 1 M NaCl was used to elute bound protein. RT-C8 typically eluted at 0.5 M NaCl. The protein was exchanged into 2× polymerase storage buffer [1 M KCl, 2 mM EDTA, and 20 mM Tris-HCl (pH 7.4)] by filter dialysis (Amicon Ultra-15 centrifugal filter unit, 50 kDa cutoff, MerckMillipore) and stored in 50% glycerol at –20 °C.

**In Vitro RNA Transcript Synthesis and Folding.** DNA templates (IDT) for all RNAs were synthesized with the addition of 5' and 3' structure cassettes.<sup>5</sup> RNAs were transcribed *in vitro* with T7 polymerase [40 mM Tris (pH 8.0), 25 mM MgCl<sub>2</sub>, 2.5 mM spermidine, 0.01% (v/v) Triton X-100, 10 mM DTT, NTPs (2.5 mM each), 15 ng/μL polymerase chain reaction (PCR)-generated template, and 0.05 mg/mL T7 RNA polymerase at 37 °C for 4 h], and the RNA product was treated with TURBO DNase (Invitrogen). Products were purified and exchanged into 0.5× TE buffer [5 mM Tris (pH 8.0) and 0.5 mM EDTA; RNAClean XP beads, Agencourt]. RNAs were refolded by being heated for 1 min at 95 °C, placed on ice for 5 min, and incubated at 37 °C for 30 min. Folding buffers were: P546 intron domain [100 mM HEPES (pH 7.5), 100 mM NaCl, and 10 mM MgCl<sub>2</sub>],<sup>45</sup> M-Box riboswitch and RNase P catalytic domain [100 mM HEPES (pH 8.0), 100 mM NaCl, and 10 mM MgCl<sub>2</sub>],<sup>52</sup> VS ribozyme [200 mM HEPES (pH 8.0), 50 mM KCl, and 10 mM MgCl<sub>2</sub>],<sup>53</sup> and group II intron [90 mM HEPES (pH 8.0), 90 mM KCl, and 115 mM MgCl<sub>2</sub>].<sup>45</sup>

**Visualization of Cross-Linked RNA by Gel Electrophoresis.** Folded RNA (either RNase P or VS ribozyme) was treated with 1/10 volume of 40 mM TBIA dissolved in DMSO, IA dissolved in DMSO, or neat DMSO and incubated at 37 °C for 15 min. Reactions were performed at 0.5 μM for RNase P and 0.5, 1.0, 1.5, and 2.0 μM for VS RNA. Reaction mixtures were purified using a G-50 spin column (GE Healthcare). Aliquots normalized to 200 ng of RNA each were denatured in an equal volume of loading buffer [95% deionized formamide, 0.025% (w/v) bromophenol blue, 0.025% (w/v) xylene cyanol, and 5 mM EDTA] at 95 °C for 2 min. The denatured RNA was loaded into a denaturing acrylamide gel (6% TBE-urea, ThermoFisher) and resolved in 1× TBE running buffer [89 mM Tris-borate (pH 8.3) and 2 mM EDTA] at 180 V for 2 or 1 h for the RNase P or VS RNAs, respectively. The gel was stained (30 min with 1× GelStar stain in TBE, Lonza) and imaged using a UV transilluminator, using a non-saturating exposure.

**Cross-Linking, Reverse Transcription, and Sequencing Library Preparation.** After folding, 5 pmol of RNA in folding buffer was added to 40 mM TBIA, IA, or neat DMSO at a 10:1 volume ratio. The samples were incubated at 37 °C for 15 min for TBIA, 30 min for IA, and 30 min for no-reagent controls; the incubation times were chosen to be five half-lives of the reagent. Samples were desalted (G-50 spin columns, GE Healthcare). RNAs were incubated with 10 pmol of a primer specific to the 3' structure cassette<sup>5</sup> at 95 °C for 1 min and



then placed on ice. Samples were then subjected to reverse transcription [20 mM Tris-HCl (pH 8.8), 10 mM  $(\text{NH}_4)_2\text{SO}_4$ , 10 mM KCl, 2 mM  $\text{MgCl}_2$ , 0.1% (v/v) Triton X-100, 200  $\mu\text{M}$  dNTPs, and 0.04 mg/mL RT-C8] at 65 °C for 4 h. Samples were desalted (G-50 spin column, GE Healthcare). The cDNA product was amplified and barcoded via a two-step PCR approach<sup>52</sup> using a high-fidelity DNA polymerase (Q5 hot-start, NEB). In step 1, 12  $\mu\text{L}$  of the 50  $\mu\text{L}$  reverse transcription reaction mixture was amplified in a 50  $\mu\text{L}$  PCR for 25 cycles with forward and reverse primers containing Illumina sequencing adapters. The excess primer was removed (DNA beads at a 1:1 sample:bead ratio; Ampure DNA Beads, Agencourt). In step 2, the product of step 1 was diluted to 0.5 ng/ $\mu\text{L}$ , and 1 ng was subjected to a 10-cycle PCR using primers complementary to Illumina sequencing adapters that contained TruSeq (Illumina) barcodes to differentiate samples in the sequencer. Short products were removed prior to sequencing (Ampure DNA beads, Agencourt; 1:1 sample:bead ratio).

To identify an optimal RT enzyme, the steps described above were performed for a diverse group of reverse transcriptase enzymes, including MMLV-M (a mutant of MMLV reverse transcriptase with activity similar to that of SuperScript II), Marathon RT,<sup>18</sup> RT521K,<sup>15</sup> and RT-C8,<sup>14</sup> except that NMIA was used as the monoadduct control. Reverse transcriptase conditions were modified to correspond to the reported optimum for each enzyme. For MMLV-M, modified SHAPE-MaP reverse transcription conditions were used.<sup>52</sup> Treated RNA (7 pmol) was incubated with 2 pmol of the 3' structure cassette<sup>5</sup> primer and 2  $\mu\text{mol}$  of dNTPs at 65 °C for 5 min and then cooled to 4 °C for 2 min. The RNA/primer mixture was incubated for 2 min at 25 °C in reverse transcription buffer, and then MMLV-M was added [final conditions of 50 mM Tris-HCl (pH 8.0), 75 mM KCl, 10 mM DTT, 1 M betaine, 6 mM  $\text{MnCl}_2$ , and 0.05 mg/mL MMLV-M]. Reverse transcription proceeded for 90 min at 42 °C followed by 10 cycles of 2 min at 50 °C and 2 min at 42 °C. The reaction was stopped by heating the mixture to 70 °C for 10 min. For Marathon, a modified version of reported reverse transcription conditions was used;<sup>18</sup> 0.25 pmol of treated RNA was incubated with 0.2 pmol of the 3' structure cassette<sup>5</sup> primer at 95 °C for 30 s and placed on ice. The incubated RNA-primer was then subjected to reverse transcription [50 mM Tris-HCl (pH 8.0), 100 mM KCl, 2 mM  $\text{MgCl}_2$ , 5 mM DTT, 500  $\mu\text{M}$  dNTPs, and 0.5  $\mu\text{M}$  MarathonRT] at 42 °C for 1 h. The reaction was stopped by heating the mixture in 300 mM NaOH at 95 °C for 5 min, and the reaction mixture was neutralized with an equivalent amount of HCl. For RT521K, the reverse transcription reaction was identical to that for RT-C8 except that 2 mM  $\text{MnCl}_2$  was substituted for 2 mM  $\text{MgCl}_2$ .

**Sequencing and Data Analysis.** Samples were sequenced on an Illumina MiSeq instrument using a 300-nucleotide kit for P546, M-Box, and VS RNAs, a 500-nucleotide kit for RNase P, and a 600-nucleotide kit for the group II intron; kit sizes provided full coverage of the target sequence. A minimum read depth of 500000 was achieved for all samples. FASTQ files were trimmed, left to right, of nucleotides with an average Q score of  $\leq 10$  in a window of five nucleotides, as described.<sup>52</sup> Reads were aligned with BWA-MEM.<sup>54</sup> Custom Python scripts were used to identify deletions of >10 nucleotides. Deletion counts were normalized by the square root of the square of median read depth across a five-nucleotide window at the 5' and 3' ends of the deletion; the rate of a given deletion in the

control sample was subtracted from the deletion rate in the cross-linked sample. The M-Box RNA was examined in this work (see Figure S2A) but had a prohibitively low deletion rate and was excluded from further analyses. All computational analysis tools were packaged into a single pipeline; scripts are available at [weekslab.com](http://weekslab.com) or [Github.com/Weeks-UNC](https://github.com/Weeks-UNC). Full independent replicates of all SHAPE-JuMP experiments were performed in parallel. Replicates were reproducible as determined by comparing overall deletion rates (Figure S2A), correlation between individual deletion rates and locations, and analyzing three-dimensional distance distributions (Figure S4) between replicate samples.

**Analysis of the Significance of Through-Space Distance Measurements.** Random sampling was used to assess whether the observed distributions of three-dimensional cross-linking distances were distinct from the distribution of distances based on random interactions of nucleotides as positioned in the RNA tertiary structure. For each RNA, 1 million random internucleotide distances were sampled from the reference structure. The random internucleotide distances were sampled such that the distribution of sequence lengths followed the same deletion length distribution as observed for the most frequent 3% of TBIA-induced deletions. A Kolmogorov–Smirnov test was performed to test if the sampled and experimentally observed distance distributions were significantly distinct from each other, as quantified by the *D* statistic. *D* measures the degree of separation between two distributions on a scale of 0–1, where a value of 0 indicates that the two sample distributions are sampled from the same population distribution and a value of 1 indicates that the two distributions are distinct.

**Restraint-Directed Three-Dimensional Structure Modeling.** Three-dimensional RNA structure modeling was performed using the DMD iFoldRNA framework.<sup>55</sup> We have used this framework for prior (no-restraint) entries in the RNA-Puzzles competitions.<sup>21,25</sup> Models for all RNAs were generated identically, with the exception that DMD steps were doubled for the group II intron RNA, due to its larger size. Modeling was performed in three steps. In step 1, a linear, unstructured model was generated, composed of all residues in the RNA, in which each nucleotide was represented by beads for the phosphate, ribose, and nucleobase moieties. A 400000-step molecular dynamics simulation was performed with canonical base pairs restrained on the basis of the accepted secondary structure. Eight identical sets of 10 replicas were run with replica temperature factor values of 0.22, 0.24, 0.26, 0.28, 0.30, 0.32, 0.34, 0.36, 0.38, and 0.40 kT; each set had a unique random seed. Structures extracted from all eight sets were ranked on the basis of free energies, and the 1% lowest-free energy structures were clustered using a 15 Å RMSD cutoff. The centroids of the eight largest clusters were then used to seed the eight replica sets of the next step. Step 2 was performed with the same parameters as step 1, except that the number of modeling iterations was reduced to 200000 and SHAPE-JuMP internucleotide interactions at multihelix and external junctions were applied as energy bonuses (Figure 7B). Internucleotide interactions between single-stranded regions of a junction or between a single-stranded region and a closing junction base pair were ascribed to the energy bonus (of  $-0.12$  kcal/mol) when the paired nucleotides were within 30 and 35 Å, respectively (see Figure 7C). Internucleotide distances used as restraints were filtered by secondary structure proximity<sup>7</sup> to prevent artifactual disruption of base pairs by the restraints.

Briefly, each SHAPE-JuMP contact was defined as nucleotide positions  $n_i$  and  $n_j$ , and compared against all base pairs, with each base pair defined as positions  $m_i$  and  $m_j$ . If  $|n_i - m_i| + |n_j - m_j| \leq 4$ , the contact was not included.<sup>7</sup> An energy bonus was also applied to each of the first three base pairs for those helices branching from a junction (Figure 7B, green lines). Bonuses were applied to base pairs within 8.6–8.9 Å. Step 3 was executed in a manner similar to that of step 2, with the addition that high-frequency tertiary SHAPE-JuMP internucleotide interactions were included as restraints. Nucleotides involved in SHAPE-JuMP interactions within the most frequent 5%, 3%, 1%, and 0.5% of deletion rates were awarded an energy bonus when participating nucleotides were within 50, 45, 40, and 35 Å, respectively (Figure 7C and Figure S5). These contacts were filtered by secondary structure proximity, as described above, using a distance of 11 instead of 4; this step removed restraints that reflect local secondary structure rather than tertiary structure. At the end of step 3, the 1% lowest-free energy structures were extracted from the eight replica simulations. A representative model was selected by mapping the SHAPE-JuMP (deletion) restraints onto these low-energy structures, and the five models with the shortest restraint distance range (largest minus shortest distance in the model, calculated from those detected by SHAPE-JuMP) were subjected to all-atom reconstruction<sup>55,56</sup> and aligned with the accepted reference structure (Figure 7D–G). We also analyzed the final models by a more conventional approach and clustered the low-energy structures using an RMSD cutoff equal to the sequence length divided by 10, as described previously.<sup>57</sup> The centroid structure of the largest cluster was aligned to the accepted reference structure.

**RMSD Calculations.** RMSD values for RNA structures modeled using SHAPE-JuMP restraints were calculated using the standard definition of the RMSD based on the positions of all atoms

$$\text{RMSD} = \sqrt{\frac{\sum_i d_i^2}{n}}$$

and based on normalizing this value to an RNA of 100 nucleotides (RMSD<sub>100</sub>):<sup>33</sup>

$$\text{RMSD}_{100} = \frac{\text{RMSD}}{-1.3 + 0.5 \ln n}$$

where  $d$  is the distance between a pair of equivalent atoms and  $n$  is the total number of atoms in the structure. The latter metric facilitates comparison of modeling results for RNAs of differing lengths.

## ■ ASSOCIATED CONTENT

### SI Supporting Information

The Supporting Information is available free of charge at <https://pubs.acs.org/doi/10.1021/acs.biochem.1c00270>.

One table and six figures (PDF)

## ■ AUTHOR INFORMATION

### Corresponding Author

Kevin M. Weeks – Department of Chemistry, The University of North Carolina at Chapel Hill, Chapel Hill, North Carolina 27599-3290, United States; [orcid.org/0000-0002-6748-9985](https://orcid.org/0000-0002-6748-9985); Email: [weeks@unc.edu](mailto:weeks@unc.edu)

## Authors

Thomas W. Christy – Department of Chemistry, The University of North Carolina at Chapel Hill, Chapel Hill, North Carolina 27599-3290, United States; Curriculum in Bioinformatics and Computational Biology, The University of North Carolina at Chapel Hill, Chapel Hill, North Carolina 27599, United States

Catherine A. Giannetti – Department of Chemistry, The University of North Carolina at Chapel Hill, Chapel Hill, North Carolina 27599-3290, United States

Gillian Houlihan – MRC Laboratory of Molecular Biology, Cambridge CB2 0QH, U.K.

Matthew J. Smola – Department of Chemistry, The University of North Carolina at Chapel Hill, Chapel Hill, North Carolina 27599-3290, United States

Gregory M. Rice – Department of Chemistry, The University of North Carolina at Chapel Hill, Chapel Hill, North Carolina 27599-3290, United States

Jian Wang – Department of Pharmacology and Department of Biochemistry and Molecular Biology, Penn State College of Medicine, Hershey, Pennsylvania 17033, United States

Nikolay V. Dokholyan – Department of Pharmacology and Department of Biochemistry and Molecular Biology, Penn State College of Medicine, Hershey, Pennsylvania 17033, United States; Department of Chemistry and Department of Biomedical Engineering, The Pennsylvania State University, University Park, Pennsylvania 16802, United States; [orcid.org/0000-0002-8225-4025](https://orcid.org/0000-0002-8225-4025)

Alain Laederach – Department of Biology, The University of North Carolina at Chapel Hill, Chapel Hill, North Carolina 27599, United States

Philipp Holliger – MRC Laboratory of Molecular Biology, Cambridge CB2 0QH, U.K.; [orcid.org/0000-0002-3440-9854](https://orcid.org/0000-0002-3440-9854)

Complete contact information is available at:

<https://pubs.acs.org/10.1021/acs.biochem.1c00270>

## Funding

This work was supported by the National Institutes of Health (NIH) (R35 GM122532 and R01 AI068462 to K.M.W., R35 GM134864 to N.V.D., and R01 GM101237 and R01 HL111527 to A.L.), the Medical Research Council (Program Grant MC\_U105178804 to P.H. and G.H.), and the Passan Foundation (to N.V.D.). T.W.C. and C.A.G. were supported in part by NIH training grants in bioinformatics (T32 GM067553) and molecular biophysics (T32 GM008570), respectively. M.J.S. was a National Science Foundation Graduate Research Fellow (DGE-1144081) and was supported in part by an NIH training grant in molecular biophysics (T32 GM08570).

## Notes

The authors declare the following competing financial interest(s): K.M.W. is an advisor to and holds equity in Ribometrix. M.J.S. is an employee of Ribometrix. Supporting data sets contain deletion locations and rates for all RNAs, for replicate experiments; restraints for DMD simulations with final model centroids; and Pymol session files showing SHAPE-JuMP data superimposed on accepted structures and the resulting DMD structure models (from Figures 6 and 7). Supporting data sets are available at <https://weekslab.com/>. Sequencing data have been deposited in sequence read archive PRJNA687281.

## ACKNOWLEDGMENTS

The authors thank S. Bozal for the initial design of the small RNA constructs.

## REFERENCES

- (1) Cech, T. R., and Steitz, J. A. (2014) The noncoding RNA revolution—trashing old rules to forge new ones. *Cell* 157, 77–94.
- (2) Mortimer, S. A., Kidwell, M. A., and Doudna, J. A. (2014) Insights into RNA structure and function from genome-wide studies. *Nat. Rev. Genet.* 15, 469–479.
- (3) Montange, R. K., and Batey, R. T. (2008) Riboswitches: emerging themes in RNA structure and function. *Annu. Rev. Biophys.* 37, 117–133.
- (4) Weeks, K. M. (2021) SHAPE directed discovery of new functions in large RNAs. *Acc. Chem. Res.* 54, 2502–2517.
- (5) Merino, E. J., Wilkinson, K. A., Coughlan, J. L., and Weeks, K. M. (2005) RNA structure analysis at single nucleotide resolution by selective 2'-hydroxyl acylation and primer extension (SHAPE). *J. Am. Chem. Soc.* 127, 4223–4231.
- (6) Siegfried, N. A., Busan, S., Rice, G. M., Nelson, J. A., and Weeks, K. M. (2014) RNA motif discovery by SHAPE and mutational profiling (SHAPE-MaP). *Nat. Methods* 11, 959–965.
- (7) Homan, P. J., Favorov, O. V., Lavender, C. A., Kursun, O., Ge, X., Busan, S., Dokholyan, N. V., and Weeks, K. M. (2014) Single-molecule correlated chemical probing of RNA. *Proc. Natl. Acad. Sci. U. S. A.* 111, 13858–13863.
- (8) Zubradt, M., Gupta, P., Persad, S., Lambowitz, A. M., Weissman, J. S., and Rouskin, S. (2017) DMS-MaPseq for genome-wide or targeted RNA structure probing in vivo. *Nat. Methods* 14, 75–82.
- (9) Mustoe, A. M., Lama, N. N., Irving, P. S., Olson, S. W., and Weeks, K. M. (2019) RNA base-pairing complexity in living cells visualized by correlated chemical probing. *Proc. Natl. Acad. Sci. U. S. A.* 116, 24574–24582.
- (10) Sengupta, A., Rice, G. M., and Weeks, K. M. (2019) Single-molecule correlated chemical probing reveals large-scale structural communication in the ribosome and the mechanism of the antibiotic spectinomycin in living cells. *PLoS Biol.* 17, No. e3000393.
- (11) Weeks, K. M. (2015) Review toward all RNA structures, concisely. *Biopolymers* 103, 438–448.
- (12) Smola, M., Calabrese, J. M., and Weeks, K. M. (2015) Detection of RNA-protein interactions in living cells with SHAPE. *Biochemistry* 54, 6867–6875.
- (13) Busan, S., Weidmann, C. A., Sengupta, A., and Weeks, K. M. (2019) Guidelines for SHAPE reagent choice and detection strategy for RNA structure probing studies. *Biochemistry* 58, 2655–2664.
- (14) Houlihan, G., Arangundy-Franklin, S., Porebski, B. T., Subramanian, N., Taylor, A. I., and Holliger, P. (2020) Discovery and evolution of RNA and XNA reverse transcriptase function and fidelity. *Nat. Chem.* 12, 683–690.
- (15) Pinheiro, V. B., Taylor, A. I., Cozens, C., Abramov, M., Renders, M., Zhang, S., Chaput, J. C., Wengel, J., Peak-Chew, S. Y., McLaughlin, S. H., Herdewijn, P., and Holliger, P. (2012) Synthetic genetic polymers capable of heredity and evolution. *Science* 336, 341–344.
- (16) Kazantsev, A. V., Krivenko, A. A., and Pace, N. R. (2009) Mapping metal-binding sites in the catalytic domain of bacterial RNase P RNA. *RNA* 15, 266–276.
- (17) Suslov, N. B., DasGupta, S., Huang, H., Fuller, J. R., Lilley, D. M. J., Rice, P. A., and Piccirilli, J. A. (2015) Crystal structure of the Varkud satellite ribozyme. *Nat. Chem. Biol.* 11, 840–846.
- (18) Zhao, C., Liu, F., and Pyle, A. M. (2018) An ultraprocesive, accurate reverse transcriptase encoded by a metazoan group II intron. *RNA* 24, 183–195.
- (19) Cate, J. H., Gooding, A. R., Podell, E., Zhou, K., Golden, B. L., Kundrot, C. E., Cech, T. R., and Doudna, J. A. (1996) Crystal structure of a group I ribozyme domain: Principles of RNA packing. *Science* 273, 1678–1685.
- (20) Toor, N., Keating, K. S., Fedorova, O., Rajashankar, K., Wang, J., and Pyle, A. M. (2010) Tertiary architecture of the *Oceanobacillus ihenyensis* group II intron. *RNA* 16, 57–69.
- (21) Miao, Z., Adamiak, R. W., Antczak, M., Batey, R. T., Becka, A. J., Biesiada, M., Boniecki, M. J., Bujnicki, J. M., Chen, S.-J., Cheng, C. Y., Chou, F.-C., Ferre-D'Amare, A. R., Das, R., Dawson, W. K., Ding, F., Dokholyan, N. V., Dunin-Horkawicz, S., Geniesse, C., Kappel, K., Kladwang, W., Krokhotin, A., Lach, G. E., Major, F., Mann, T. H., Magnus, M., Pachulska-Wieczorek, K., Patel, D. J., Piccirilli, J. A., Popena, M., Purzycka, K. J., Ren, A., Rice, G. M., Santalucia, J. J., Sarzynska, J., Szachniuk, M., Tandon, A., Trausch, J. J., Tian, S., Wang, J., Weeks, K. M., Williams, B., 2nd, Xiao, Y., Xu, X., Zhang, D., Zok, T., and Westhof, E. (2017) RNA-Puzzles Round III: 3D RNA structure prediction of five riboswitches and one ribozyme. *RNA* 23, 655–672.
- (22) Christy, T. W., Giannetti, C. A., Laederach, A., and Weeks, K. M. Identifying proximal RNA interactions from cDNA-encoded crosslinks with ShapeJumper. *bioRxiv* 2021.06.10.447916.
- (23) Fang, X. W., Pan, T., and Sosnick, T. R. (1999) Mg<sup>2+</sup>-dependent folding of a large ribozyme without kinetic traps. *Nat. Struct. Biol.* 6, 1091–1095.
- (24) McGinnis, J. L., Dunkle, J. A., Cate, J. H. D., and Weeks, K. M. (2012) The mechanisms of RNA SHAPE chemistry. *J. Am. Chem. Soc.* 134, 6617–6624.
- (25) Miao, Z., Adamiak, R. W., Antczak, M., Boniecki, M. J., Bujnicki, J., Chen, S.-J., Cheng, C. Y., Cheng, Y., Chou, F.-C., Das, R., Dokholyan, N. V., Ding, F., Geniesse, C., Jiang, Y., Joshi, A., Krokhotin, A., Magnus, M., Mailhot, O., Major, F., Mann, T. H., Piątkowski, P., Pluta, R., Popena, M., Sarzynska, J., Sun, L., Szachniuk, M., Tian, S., Wang, J., Wang, J., Watkins, A. M., Wiedemann, J., Xiao, Y., Xu, X., Yesselman, J. D., Zhang, D., Zhang, Y., Zhang, Z., Zhao, C., Zhao, P., Zhou, Y., Zok, T., Żyła, A., Ren, A., Batey, R. T., Golden, B. L., Huang, L., Lilley, D. M., Liu, Y., Patel, D. J., and Westhof, E. (2020) RNA-Puzzles Round IV: 3D structure predictions of four ribozymes and two aptamers. *RNA* 26, 982–995.
- (26) Ponce-Salvaterra, A., Astha, Merdas, K., Nithin, C., Ghosh, P., Mukherjee, S., and Bujnicki, J. M. (2019) Computational modeling of RNA 3D structure based on experimental data. *Biosci. Rep.* 39, 39.
- (27) Li, B., Cao, Y., Westhof, E., and Miao, Z. (2020) Advances in RNA 3D structure modeling using experimental data. *Front. Genet.* 11, 574485.
- (28) Ding, F., Sharma, S., Chalasani, P., Demidov, V. V., Broude, N. E., and Dokholyan, N. V. (2008) Ab initio RNA folding by discrete molecular dynamics: from structure prediction to folding mechanisms. *RNA* 14, 1164–1173.
- (29) Gherghe, C. M., Leonard, C. W., Ding, F., Dokholyan, N. V., and Weeks, K. M. (2009) Native-like RNA tertiary structures using a sequence-encoded cleavage agent and refinement by discrete molecular dynamics. *J. Am. Chem. Soc.* 131, 2541–2546.
- (30) Brion, P., and Westhof, E. (1997) Hierarchy and dynamics of RNA folding. *Annu. Rev. Biophys. Biomol. Struct.* 26, 113–137.
- (31) Hajdin, C. E., Bellaousov, S., Huggins, W., Leonard, C. W., Mathews, D. H., and Weeks, K. M. (2013) Accurate SHAPE-directed RNA secondary structure modeling, including pseudoknots. *Proc. Natl. Acad. Sci. U. S. A.* 110, 5498–5503.
- (32) Beattie, T. L., Olive, J. E., and Collins, R. A. (1995) A secondary-structure model for the self-cleaving region of *Neurospora* VS RNA. *Proc. Natl. Acad. Sci. U. S. A.* 92, 4686–4690.
- (33) Carugo, O., and Pongor, S. (2001) A normalized root-mean-square distance for comparing protein three-dimensional structures. *Protein Sci.* 10, 1470–1473.
- (34) Toor, N., Keating, K. S., Taylor, S. D., and Pyle, A. M. (2008) Crystal structure of a self-spliced group II intron. *Science* 320, 77–82.
- (35) Lu, Z., Zhang, Q. C., Lee, B., Flynn, R. A., Smith, M. A., Robinson, J. T., Davidovich, C., Gooding, A. R., Goodrich, K. J., Mattick, J. S., Mesirov, J. P., Cech, T. R., and Chang, H. Y. (2016) RNA duplex map in living cells reveals higher-order transcriptome structure. *Cell* 165, 1267–1279.

- (36) Aw, J. G. A., Shen, Y., Wilm, A., Sun, M., Lim, X. N., Boon, K.-L., Tapsin, S., Chan, Y.-S., Tan, C.-P., Sim, A. Y. L., Zhang, T., Susanto, T. T., Fu, Z., Nagarajan, N., and Wan, Y. (2016) In vivo mapping of eukaryotic RNA interactomes reveals principles of higher-order organization and regulation. *Mol. Cell* 62, 603–617.
- (37) Sharma, E., Sterne-Weiler, T., O'Hanlon, D., and Blencowe, B. J. (2016) Global mapping of human RNA-RNA interactions. *Mol. Cell* 62, 618–626.
- (38) Ziv, O., Gabryelska, M. M., Lun, A. T. L., Gebert, L. F. R., Sheu-Gruttadauria, J., Meredith, L. W., Liu, Z.-Y., Kwok, C. K., Qin, C.-F., MacRae, I. J., Goodfellow, I., Marion, J. C., Kudla, G., and Miska, E. A. (2018) COMRADES determines in vivo RNA structures and interactions. *Nat. Methods* 15, 785–788.
- (39) Weidmann, C. A., Mustoe, A. M., and Weeks, K. M. (2016) Direct duplex detection: An emerging tool in the RNA structure analysis toolbox. *Trends Biochem. Sci.* 41, 734–736.
- (40) Graveley, B. R. (2016) RNA matchmaking: Finding cellular pairing partners. *Mol. Cell* 63, 186–189.
- (41) Lu, Z., and Chang, H. Y. (2018) The RNA base-pairing problem and base-pairing solutions. *Cold Spring Harbor Perspect. Biol.* 10, a034926.
- (42) Kladwang, W., VanLang, C. C., Cordero, P., and Das, R. (2011) A two-dimensional mutate-and-map strategy for non-coding RNA structure. *Nat. Chem.* 3, 954–962.
- (43) Homan, P. J., Tandon, A., Rice, G. M., Ding, F., Dokholyan, N. V., and Weeks, K. M. (2014) RNA tertiary structure analysis by 2'-hydroxyl molecular interference. *Biochemistry* 53, 6825–6833.
- (44) Cheng, C. Y., Chou, F.-C., Kladwang, W., Tian, S., Cordero, P., and Das, R. (2015) Consistent global structures of complex RNA states through multidimensional chemical mapping. *eLife* 4, No. e07600.
- (45) Ding, F., Lavender, C. A., Weeks, K. M., and Dokholyan, N. V. (2012) Three-dimensional RNA structure refinement by hydroxyl radical probing. *Nat. Methods* 9, 603–608.
- (46) Kerpedjiev, P., Höner Zu Siederdisen, C., and Hofacker, I. L. (2015) Predicting RNA 3D structure using a coarse-grain helix-centered model. *RNA* 21, 1110–1121.
- (47) Costa, M., Michel, F., and Westhof, E. (2000) A three-dimensional perspective on exon binding by a group II self-splicing intron. *EMBO J.* 19, 5007–5018.
- (48) Dai, L., Chai, D., Gu, S.-Q., Gabel, J., Noskov, S. Y., Blocker, F. J. H., Lambowitz, A. M., and Zimmerly, S. (2008) A three-dimensional model of a group II intron RNA and its interaction with the intron-encoded reverse transcriptase. *Mol. Cell* 30, 472–485.
- (49) Gardner, A. F., and Jack, W. E. (2002) Acyclic and dideoxy terminator preferences denote divergent sugar recognition by archaeon and Taq DNA polymerases. *Nucleic Acids Res.* 30, 605–613.
- (50) Fogg, M. J., Pearl, L. H., and Connolly, B. A. (2002) Structural basis for uracil recognition by archaeal family B DNA polymerases. *Nat. Struct. Biol.* 9, 922–927.
- (51) Ramsay, N., Jemth, A. S., Brown, A., Crampton, N., Dear, P., and Holliger, P. (2010) CyDNA: synthesis and replication of highly Cy-dye substituted DNA by an evolved polymerase. *J. Am. Chem. Soc.* 132, 5096–5104.
- (52) Smola, M. J., Rice, G. M., Busan, S., Siegfried, N. A., and Weeks, K. M. (2015) Selective 2'-hydroxyl acylation analyzed by primer extension and mutational profiling (SHAPE-MaP) for direct, versatile and accurate RNA structure analysis. *Nat. Protoc.* 10, 1643–1669.
- (53) Hiley, S. L., and Collins, R. A. (2001) Rapid formation of a solvent-inaccessible core in the *Neurospora* Varkud satellite ribozyme. *EMBO J.* 20, 5461–5469.
- (54) Li, H., and Durbin, R. (2010) Fast and accurate long-read alignment with Burrows-Wheeler transform. *Bioinformatics* 26, 589–595.
- (55) Krokhotin, A., Houlihan, K., and Dokholyan, N. V. (2015) iFoldRNA v2: folding RNA with constraints. *Bioinformatics* 31, 2891–2893.
- (56) Sharma, S., Ding, F., and Dokholyan, N. V. (2008) iFoldRNA: three-dimensional RNA structure prediction and folding. *Bioinformatics* 24, 1951–1952.
- (57) Boniecki, M. J., Lach, G., Dawson, W. K., Tomala, K., Lukasz, P., Soltysinski, T., Rother, K. M., and Bujnicki, J. M. (2016) SimRNA: a coarse-grained method for RNA folding simulations and 3D structure prediction. *Nucleic Acids Res.* 44, No. e63.